

Topology optimization for metastructures with quasi-zero stiffness and snap-through features

Yifu Lu^{*}, Quantian Luo, Liyong Tong^{*}

School of Aerospace, Mechanical and Mechatronic Engineering, The University of Sydney, Sydney, NSW 2006, Australia

ARTICLE INFO

Keywords:

Quasi-zero stiffness
Metastructure
Topology optimization
Nonlinear finite element analysis
Snap-through

ABSTRACT

Quasi-zero stiffness (QZS) is highly demanded in passive vibration isolators. Most of the existing design methods of QZS vibration isolators are typically based on mechanism designs, where pre-defined structural configurations, components, or mechanisms with certain features, such as negative stiffness, are required to synthesize the designs. This work introduces topology optimization for QZS structure designs, enabling the design of structures without pre-definitions and resulting in single-part designs rather than structural assemblies. We propose novel mathematical formulations of the objective function based on the QZS force-displacement curve and generic mathematical formulations of the optimization problem. An extended moving isosurface threshold method is used to solve the formulated optimization problem. In addition, topology optimization of metastructures with snap-through features and an alternative design method that synthesizes QZS metastructures by combining snap-through structures with positive stiffness elements are also presented. The optimized snap-through metastructures are numerically validated by nonlinear finite element analysis (NFEA) and experiment, which shows negative stiffness and snap-through characteristics. Numerical examples and investigations are presented for the QZS structures designed by both optimization and synthesis methods. The NFEA results reveal the QZS designs obtained from the two methods can achieve approximately constant stiffness of 0.502 N/mm over a 17 mm displacement range and 0.402 N/mm over a 12 mm displacement range, respectively.

1. Introduction

Vibration control aims to effectively reduce or minimize the undesirable and harmful effects caused by vibrations, which is crucial in many engineering fields and the natural world [1–3]. One of the most common methods of passive vibration control is to use a system to isolate the transmission between the vibration source and the object being controlled. Quasi-zero stiffness (QZS) vibration isolation is a typical nonlinear passive vibration isolation technique to isolate vibration with ultralow frequency, which cannot be achieved by a linear vibration isolation system [4]. It also has a wider vibration isolation frequency band as compared to a linear isolator due to its high-static and low-dynamic stiffness.

Structures with QZS features can be achieved via mechanism designs, where the most notable approach is to combine positive and negative stiffness elements. A variety of negative stiffness elements have been studied, with the oblique springs [5] being a common type. As compared to the QZS isolator with one pair of oblique springs [5], the isolators with two pairs [6] and three pairs [7] of oblique

^{*} Corresponding authors.

E-mail addresses: yifu.lu@sydney.edu.au (Y. Lu), liyong.tong@sydney.edu.au (L. Tong).

springs offer wider QZS regions, and the QZS isolator with three pairs of oblique springs [7] exhibits lower transmissibility. Other typical negative stiffness elements in the literature include, but are not limited to, X-shaped structures [8,9], curved beams [10,11], buckled beams [12,13], magnets [14,15], cam-roller-spring mechanisms [16,17], bistable mechanisms [18,19] and multibody system [20]. Some QZS device designs based on metamaterials [21–23], metastructures [24,25], conical shells [26,27], bio-inspired structures [28], and other structures and mechanisms [29] are also developed.

It is evident that the existing designs of QZS vibration isolation systems based on the mechanism design require certain pre-defined structures or mechanisms with negative stiffness characteristics, and the designs or prototypes are derived based on these mechanisms. By contrast, topology optimization studies the optimal geometry configuration and material distribution in a design domain with specific constraints, without pre-definition of structural configurations. In addition, the majority of the existing designs are structural assemblies, while structural designs obtained via topology optimization are single-part designs.

Topology optimization for metamaterials or metastructures has attracted vast research interests in recent years. Properties of metamaterials change with the configuration of their base cells rather than with composition, and their peculiar physical properties are not found in nature usually. For example, metamaterials with negative permeability [30–32], negative Poisson's ratio [33,34], and extreme elastic modulus [35,36] were studied. In addition, other functionalities were also achieved, such as cloaking [37–39], microwave absorption [40] and vibration suppression [41]. Recently, QZS metastructures were designed by structural optimization via genetic algorithm [42], in which a heuristic searching method was applied. However, there has been a lack of attempts to develop mathematical formulations for the topology optimization of QZS metastructures, as well as methods and algorithms to solve the optimization problem. This work aims to introduce the topology optimization method to formulate and solve the QZS topology optimization problem, where the distinctive feature in comparison with the existing design method is the present method does not require pre-defined structural configurations.

Moreover, this paper also considers an alternative design method that synthesizes QZS metastructures by combining positive and negative stiffness elements. Inspired by the bistable mechanisms [18,19] with snap-through features as the negative stiffness element, we extend our previous work [43] to solve topology optimization of structures with snap-through features [44–49] and use the optimized structures as the negative stiffness element. Subsequently, the snap-through metastructures are combined with a simple bar as the positive stiffness element to form QZS metastructures.

This study proposes a topology optimization method for QZS metastructures, including novel and generic mathematical formulations and an extended moving isosurface threshold (MIST) method to solve the formulated optimization problem. In addition, topology optimization of metastructures with snap-through features [43] is further investigated. The objective functions are defined based on the force-displacement curve, and the optimization problems are formulated using displacement and reaction force in terms of stress and strain of all load steps in nonlinear finite element analysis (NFEA). Numerical examples are provided to verify the present formulation and algorithm. The optimized designs are validated by NFEA and/or experiment for QZS or snap-through behaviors.

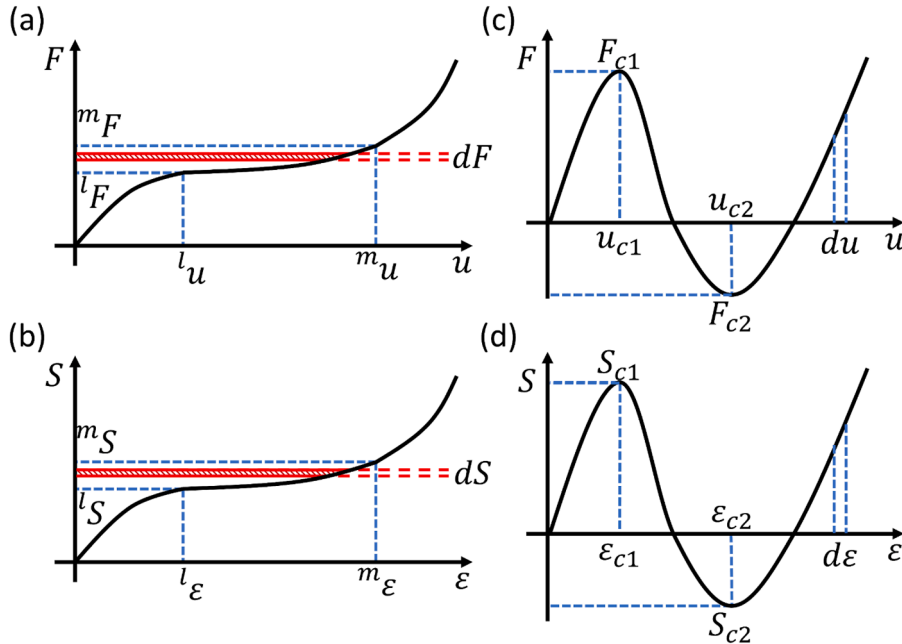


Fig. 1. Schematic relationships of force-displacement and stress-strain of structures with (a, b) QZS and (c, d) snap-through features, where u and F denote the displacement and force; ϵ and S represent the Green-Lagrange strain and second Piola-Kirchhoff stress; superscripts l and m indicate the lower and upper bounds of the QZS region; and subscripts $c1$ and $c2$ correspond to the critical points on F - u curves.

2. Problem formulation and algorithm

Metamaterials are often composed of multiple cells arranged in periodic patterns, where performance can be analyzed based on the behavior of the base cell. This paper focuses on the optimal design of a base cell with QZS features. This section presents the mathematical formulations of topology optimization for QZS metastructures, an optimization method and an algorithm to implement the optimization problem. Moreover, in order to design QZS metastructures using structures with snap-through features, formulations and an optimization method are also developed for this type of design problem.

2.1. Problem statement of QZS metastructures

In this section, the QZS design problem is defined using the force-displacement curve, followed by deriving the relationships between force-displacement and stress-strain based on the complementary strain energy principle, in order to formulate optimization problem for metastructures with QZS features. Let us consider a structure subjected to an enforced displacement u or a force F . The force-displacement (F - u) relationships can be illustrated in Fig. 1(a) and (c) for QZS and snap-through features. Consequently, the objective functions of QZS metastructures can be defined based on the F - u curves. The design objective of QZS metastructures is to achieve constant force in a range of displacements ($l'u \leq u \leq m'u$), as illustrated in Fig. 1(a). For a structure subjected to an enforced displacement, the design objective of the QZS characteristic is mathematically expressed as:

$$\frac{dF}{du} = 0 \quad l'u \leq u \leq m'u \quad (1)$$

where u is the displacement and F represents the reaction force at the point with the prescribed displacement.

In order to achieve the constant force, the optimization problem can be defined as minimizing the stiffness in the displacement range of $l'u \leq u \leq m'u$:

$$\min : J = \sum_{k=l+1}^m \frac{kF - k-1F}{k u - k-1u} \quad (2)$$

Thus, it is important to express the reaction force F in the objective function Eq. (2) for a structure subjected to an enforced displacement in nonlinear analysis. In this work, we derive an approximated reaction force formula in terms of stress and strain histories. For simplicity in the derivations and formulations, instead of considering the variational principle of complementary work for the elastic body, only loading increments are considered, in which the force-displacement and stress-strain curves can be treated as piecewise linear; in this case, the work done by the enforced displacement and the complementary strain energy are thus approximately equivalent. The detailed derivations are as follows.

When a structure with the QZS or snap-through feature is subjected to enforced displacement u or force F , force-displacement and stress-strain relationships can be described in Fig. 1, which reveals that the structural analysis could be highly nonlinear. The nonlinear structural analysis could be conducted by incrementally applying external loading (F or u) to the structure. When the loading is expressed as a function of time, the approximated equivalence of the work done by the enforced displacement and the complementary strain energy for nonlinear structures can be expressed as:

$$\int_{0\Omega}^{(t+\Delta t)} u_i \delta f_i^b d^0\Omega + \int_{0S}^{(t+\Delta t)} u_i \delta f_i^s d^0S + \int_{0\Omega}^{(t+\Delta t)} u_i \delta f_i^c = \int_{0\Omega}^{(t+\Delta t)} \epsilon_{ij} \delta S_{ij} d^0\Omega \quad (3)$$

where S_{ij} and ϵ_{ij} denote the second Piola-Kirchhoff stress and Green-Lagrange strain tensors; f_i^b , f_i^s and f_i^c are tensors of the body force, surface traction and concentrated force; u_i is the displacement tensor; 0Ω and $0S$ represent the structural volume and surface area at time $t = 0$.

Eq. (3) can be written in the total Lagrangian formulation of NFEA as:

$${}^k u \delta F = \int_{0\Omega} {}^k \epsilon_{ij} \delta S_{ij} d^0\Omega \quad (k = 1, 2, \dots, n) \quad (4)$$

where F and u represent the force and displacement vectors; superscripts k and n denote the k^{th} load increment and the total number of load increments in NFEA.

Subsequently, the left-hand side of Eq. (2) is integrated over the loading increment $dF = {}^k F - {}^{k-1} F$, and the right-hand side is integrated over the increment $dS_{ij} = {}^k S_{ij} - {}^{k-1} S_{ij}$, as shown in Fig. 1(a) and (b). By assuming the force-displacement and stress-strain curves are piecewise linear in the segments dF and dS_{ij} and applying the trapezoidal rule to evaluate the integrals, the trapezoid areas of both integrals (shaded in Fig. 1(a) and (b)) at synchronized load steps k ($=1, 2, \dots, n$) are equivalent:

$$\frac{1}{2} ({}^k u + {}^{k-1} u) ({}^k F - {}^{k-1} F) = \int_{0\Omega} \frac{1}{2} ({}^k \epsilon_{ij} + {}^{k-1} \epsilon_{ij}) ({}^k S_{ij} - {}^{k-1} S_{ij}) d^0\Omega \quad (5)$$

where $k = 1, 2, \dots, n$.

When the enforced displacement \mathbf{u} is only one non-zero displacement u , Eq. (5) degenerates to:

$${}^k F - {}^{k-1} F = \int_{\Omega} \left[\frac{1}{k u + {}^{k-1} u} ({}^k \varepsilon_{ij} + {}^{k-1} \varepsilon_{ij}) ({}^k S_{ij} - {}^{k-1} S_{ij}) \right] d^0 \Omega \quad (6a)$$

where ${}^k F$ is the magnitude of ${}^k \mathbf{F}$, ${}^k u$ denotes the associated displacement at the k^{th} load step, and $k = 1, 2, \dots, n$.

By the summation of Eq. (6a) for $k = l, l + 1, \dots, m-1, m$ respectively, one can obtain:

$${}^m F - {}^l F = \sum_{k=l+1}^m \int_{\Omega} \frac{1}{k u + {}^{k-1} u} ({}^k \varepsilon_{ij} + {}^{k-1} \varepsilon_{ij}) ({}^k S_{ij} - {}^{k-1} S_{ij}) d^0 \Omega \quad (6b)$$

The force formulation in Eqs. (6a) and (6b) will be used to formulate topology optimization for QZS metastructures. By using the derived force formulation Eq. (6a), the objective function Eq. (2) can be rewritten as:

$$J = \sum_{k=l+1}^m \int_{\Omega} \frac{1}{k u^2 - {}^{k-1} u^2} ({}^k \varepsilon_{ij} + {}^{k-1} \varepsilon_{ij}) ({}^k S_{ij} - {}^{k-1} S_{ij}) d^0 \Omega \quad (7)$$

When the enforced displacement is applied with an equal increment in the NFEA, one can define a constant as: ${}^k u - {}^{k-1} u = \text{constant} = d$. The objective function can be rewritten using Eq. (6b) as:

$$\begin{aligned} J &= \frac{1}{d} \sum_{k=l+1}^m ({}^k F - {}^{k-1} F) = \frac{{}^m F - {}^l F}{d} \\ &= \frac{1}{d^2} \sum_{k=l+1}^m \frac{1}{2k-1} \int_{\Omega} ({}^k \varepsilon_{ij} + {}^{k-1} \varepsilon_{ij}) ({}^k S_{ij} - {}^{k-1} S_{ij}) d^0 \Omega \end{aligned} \quad (8)$$

It is worth noting that since the enforced displacement is applied with an equal step length in the NFEA in this work, the simplified objective function Eq. (8) is used in numerical implementation and computation. However, the derivation for the generalized case Eq. (7) is also presented. The objective function in Eqs. (7) or (8) is the complementary energy with a positive constant coefficient, e.g., $1/(2k-1)d^2$, ensuring it remains non-negative. As J is minimized, it converges toward zero, resulting in QZS. It is also worth noting that the proposed objective function with equal displacement increment in Eq. (8) minimizes not only the stiffness dF/du but also the force difference $\delta F (= {}^m F - {}^l F)$ in the range of ${}^l u \leq u \leq {}^m u$. Thus, with this objective function, the stiffness achieved is both quasi-zero (F - u curve horizontal) and approximately constant (F - u curve is linear) in a range of ${}^l u \leq u \leq {}^m u$.

Thus, the optimization problem can be mathematically stated as to find \mathbf{x}_e so that:

$$\min : J(\mathbf{x}_e) = \frac{1}{d^2} \sum_{k=l+1}^m \left(\frac{{}^k \varepsilon_{ij}(\mathbf{x}_e) + {}^{k-1} \varepsilon_{ij}(\mathbf{x}_e)}{2k-1} \right) ({}^k S_{ij}(\mathbf{x}_e) - {}^{k-1} S_{ij}(\mathbf{x}_e)) d^0 \Omega \quad (9a)$$

$$\text{s.t. : } \begin{cases} {}^n \mathbf{R}_u(\mathbf{x}_e) = 0 & \text{in } {}^0 \Omega \\ \sum_{e=1}^{N_e} \mathbf{x}_e V_e - V_f V \leq 0 & \mathbf{x}_e \in {}^0 \Omega \\ 0 < x_{\min} \leq \mathbf{x}_e \leq 1 \end{cases} \quad (9b)$$

where \mathbf{x}_e is the design variable and $x_{\min} (= 10^{-3})$ represents the design variable of void material; e represents the e^{th} element and N_e is the number of total elements; V_f , V_e , and V are the volume fraction, elemental volume and the total volume of the design domain; superscript n represents the total number of load steps; ${}^n \mathbf{R}$ is the residual force vector in the final equilibrium state, and in load step k : ${}^k \mathbf{R}_u = {}^k \mathbf{F}_{eq} - {}^k \mathbf{F}_r$ ($k = 1, 2, \dots, n$), where ${}^k \mathbf{F}_r$ denotes the stress resultant; ${}^k \mathbf{R}_{eq}$ is the equivalent force vector caused by the enforced displacement.

2.2. Problem statement of metastructures with snap-through features

This section presents the formulation of the optimization problem for metastructures with snap-through features, based on the force-displacement curve and the principle of virtual work. As illustrated in Fig. 1(c), negative stiffness (see $u_{c1} \leq u \leq u_{c2}$) is a distinctive characteristic of structures with snap-through features, and a snap-through can be achieved only when the applied force is larger than its critical one ($F > F_{c1}$). Hence, the design optimization of structures with snap-through features can be defined as maximizing displacement $u(F)$ for the applied force $F > F_{c1}$. Therefore, to formulate the optimization problem, the displacement u for a structure subjected to a force in nonlinear analysis should be derived.

In order to derive the formulation of displacement for a structure subjected to a force, where state variables are displacements, the principle of virtual work for nonlinear structures may be expressed as [50]:

$$\int_{\Omega}^{(t+\Delta t)} S_{ij} \delta \varepsilon_{ij} d^0 \Omega = \int_{\Omega}^{(t+\Delta t)} f_i^b \delta u_i d^0 \Omega + \int_{\Omega}^{(t+\Delta t)} f_i^s \delta u_i d^0 S + \int_{\Omega}^{(t+\Delta t)} f_i^c \delta u_i d^0 \Omega \quad (10)$$

Eq. (10) can be expressed in the total Lagrangian formulation and integrated as:

$${}^k \mathbf{F} \delta \mathbf{u} = \int_{\Omega} {}^k S_{ij} \delta \varepsilon_{ij} d^0 \Omega \quad (k = 1, 2, \dots, n) \quad (11a)$$

$$\int_{k-1}^k \mathbf{F} d\mathbf{u} = \int_{\Omega} \left(\int_{k-1}^k S_{ij} d\varepsilon_{ij} \right) d^0 \Omega \quad (k = 1, 2, \dots, n) \quad (11b)$$

Eq. (11b) can be approximated by using the trapezoidal rule to evaluate the integral:

$$\frac{1}{2} ({}^k \mathbf{F} + {}^{k-1} \mathbf{F}) ({}^k \mathbf{u} - {}^{k-1} \mathbf{u}) = \int_{\Omega} \frac{1}{2} ({}^k S_{ij} + {}^{k-1} S_{ij}) ({}^k \varepsilon_{ij} - {}^{k-1} \varepsilon_{ij}) d^0 \Omega \quad (12)$$

where $k = 1, 2, \dots, n$.

When there is only one non-zero force \mathbf{F} in \mathbf{F} applied to the structure, Eq. (12) can be degenerated and rearranged as:

$${}^k \mathbf{u} - {}^{k-1} \mathbf{u} = \int_{\Omega} \left[\frac{1}{k\mathbf{F} + {}^{k-1}\mathbf{F}} ({}^k S_{ij} + {}^{k-1} S_{ij}) ({}^k \varepsilon_{ij} - {}^{k-1} \varepsilon_{ij}) \right] d^0 \Omega \quad (13)$$

where the load step $k = 1, 2, \dots, n$.

By the summation of Eq. (13) for $k = 1, 2, \dots, n$ respectively and assuming that ${}^0 \mathbf{u} = 0$, one can obtain:

$${}^n \mathbf{u} = \int_{\Omega} \left[\sum_{k=1}^n \left(\frac{{}^k S_{ij} + {}^{k-1} S_{ij}}{k\mathbf{F} + {}^{k-1}\mathbf{F}} \right) ({}^k \varepsilon_{ij} - {}^{k-1} \varepsilon_{ij}) \right] d^0 \Omega \quad (14)$$

where ${}^n \mathbf{u}$ represents the displacement in the final equilibrium state.

With the displacement formulation in Eq. (14), topology optimization for metastructures with snap-through feature is mathematically stated as to find \mathbf{x}_e for the applied force \mathbf{F} ($F > F_{c1}$) so that:

$$\max : J = u(\mathbf{x}_e) = \int_{\Omega} \left[\sum_{k=1}^n \left(\frac{{}^k S_{ij}(\mathbf{x}_e) + {}^{k-1} S_{ij}(\mathbf{x}_e)}{k\mathbf{F} + {}^{k-1}\mathbf{F}} \right) ({}^k \varepsilon_{ij}(\mathbf{x}_e) - {}^{k-1} \varepsilon_{ij}(\mathbf{x}_e)) \right] d^0 \Omega \quad (15a)$$

$$s.t. : \begin{cases} {}^n \mathbf{R}_F(\mathbf{x}_e) = 0 & \text{in } {}^0 \Omega \\ \sum_{e=1}^{N_e} \mathbf{x}_e V_e - V_f V \leq 0 & \mathbf{x}_e \in {}^0 \Omega \\ 0 < x_{min} \leq x_e \leq 1 \end{cases} \quad (15b)$$

where F_{c1} is the positive critical force; ${}^n \mathbf{R}_F$ is the residual force vector in the final equilibrium state, and in load step ${}^k \mathbf{R}_F = {}^k \mathbf{F}_{ex} - {}^k \mathbf{F}_r$ ($k = 1, 2, \dots, n$), where ${}^k \mathbf{F}_r$ denotes the stress resultant and ${}^k \mathbf{R}_{ex}$ is the external force vector.

It is worth noting that when $F < F_{c1}$, negative stiffness will not occur and the optimized design will not exhibit snap-through behavior; if F is too large, the NFEA computation may not converge. The applied force is required to be sufficiently large to induce negative stiffness but not large enough to diverge NFEA. Thus, the difficulties in topology optimization for structures with snap-through features include determining the applied force and handling negative stiffness computation.

2.3. Solution method

This section discusses the solutions to Eqs. (9) and (15) to present an effective solving method. The topology optimization of QZS metastructures, as formulated in Eq. (9), can potentially be solved using various methods, such as density-based or level-set methods. The sensitivity analysis or level-set function could be developed for such methods based on the proposed objective function in Eqs. (7) or (8), which may involve challenges. In this work, a moving isosurface threshold method (MIST) will be applied due to its features: clear topology representations, unnecessary explicit sensitivity formulations, and effectiveness in handling highly nonlinear problems [51] in topology optimization.

The MIST method describes and updates the structural topology by the intersection of a physical response function surface (Φ) and an isosurface threshold level (t). The objective function in MIST is typically expressed in an integral form over the design domain Ω ,

and the response function is derived as the integrand. Thus, although explicit sensitivity analysis is not performed in the MIST, the response function can provide gradient/sensitivity information (dJ/dx_e) for topology update in a similar manner, as it reflects the nodal structural/physical response with respect to the objective function in Ω . Based on the present formulation in Eq. (9), the response function of optimization for QZS metastructures can be derived as the integrand of the objective function in Eq. (9a):

$$\Phi_{QZS} = \frac{1}{d^2} \sum_{k=l+1}^m \frac{1}{2k-1} ({}^k\varepsilon_{ij} + {}^{k-1}\varepsilon_{ij}) ({}^kS_{ij} - {}^{k-1}S_{ij}) \quad (16)$$

For optimization of metastructures with snap-through features, the objective function Eq. (15a) is the final state displacement nu , which is expressed as an integral over Ω . Therefore, the response function is selected correspondingly as the integrand of Eq. (15a):

$$\Phi_u = \sum_{k=1}^n \frac{1}{kF + {}^{k-1}F} ({}^kS_{ij} + {}^{k-1}S_{ij}) ({}^k\varepsilon_{ij} - {}^{k-1}\varepsilon_{ij}) \quad (17)$$

To impose the prescribed volume fraction constraint in Eq. (9b) and (15b), the objective function Eq. (9a) or (15a) can be expressed as below [52,53], with the response function Φ being Eqs. (16) or (17).

$$J(x_e) = \int_{\Omega} \Phi(x_e) H(\Phi - t) d\Omega \quad (18)$$

where H is the Heaviside function and t is the isosurface threshold value. Once t is calculated corresponding to the prescribed volume fraction, design variables are computed by [52,53]:

$$x_e = \begin{cases} 1 & \text{if } \Phi \geq t \text{ (at all nodes of element } e) \\ 0 & \text{if } \Phi < t \text{ (at all nodes of element } e) \\ \frac{A_{epj}}{A_e} & \text{else} \end{cases} \quad (19)$$

where A_{pj} and A_e are the projection area of $\Phi \geq t$ within element e and the element area.

The optimal solutions of topologies Ω and design variables x_e can be solved by implementing the iterative process of the MIST with the response function Eqs. (16) or (17), and the implementation is detailed in the Appendix. The details can be referred to [52,53] for the basic MIST algorithm and [54] for the optimization of nonlinear structures. In the present implementation, MATLAB is employed to code the algorithm, and MSC NASTRAN is used as the FEA solver.

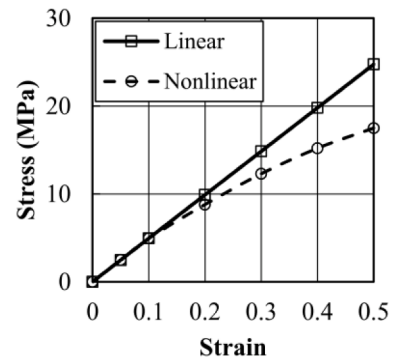
3. Numerical examples

This section presents design cases for topology optimization of metastructures with QZS or snap-through features via numerically studying the problem formulated in Eqs. (9) and (15) using the extended MIST algorithm detailed in Section 2.3. The MIST solver parameters are chosen as: initial dynamic move limit $k_{mv}^0 = 0.5$; $x_{\min} = 10^{-3}$; prescribed volume fraction $V_f = 0.2$; filter radius $r_{\min} = 4 \times \text{element size}$; and material penalty factor $p = 1$ and increases by 0.05 per iteration until reaches 3. The materials are initialized as uniformly distributed in the design domain ($x_e = V_f$), and no specified initial distribution is required. The definitions of the solver parameters and implementation are detailed in the Appendix. In the case studies, both geometrical and material nonlinearities are considered. In the NFEA, the nonlinear elasticity properties are input via tabular data, where the elasticity properties (linear and

Table 1

Material properties of polyurethane: linear and nonlinear.

Young's modulus	Poisson's ratio
49.5 MPa	0.292
Strain (m/m)	Stress (MPa)
0	0
0.05	2.48
0.10	4.95
0.20	8.80
0.30	12.30
0.40	15.20
0.50	17.50



nonlinear) of the polyurethane material used in this study are listed in Table 1.

3.1. QZS metastructures

Fig. 2(a) illustrates a QZS metastructure design case, including dimension and loading and supporting conditions. The computational model simplified using symmetry conditions is depicted in Fig. 2(b), where the dimension of the design domain is 100×50 and an 80×40 mesh is applied. It is worth noting that a fixed constraint should be imposed at the bottom point along the symmetry axis (see Fig. 2(a)). However, applying a fixed boundary condition can result in significant complementary strain energy concentration at that point, causing material accumulation in the region. In this study, we relax and approximate the fixed boundary condition with a typical flexible constraint: an artificial spring, as shown in Fig. 2(b).

In QZS design problems, an enforced displacement u is applied, as formulated in Section 2.1. The displacement u requires to be sufficiently large to induce nonlinear deformation but not too large to converge in the NFEA. Thus, the applied enforced displacement u should be carefully chosen and coupled with the artificial spring stiffness. For spring stiffness $k_{\text{Spring}} = 3 \text{ N/mm}$, three different selections $u = 17, 16$, and 15 mm are computed and presented in Fig. 3(a)–(c) respectively. For the enforced displacement $u > 17 \text{ mm}$ with $k_{\text{Spring}} = 3 \text{ N/mm}$, the nonlinear deformations are too large and the NFEA may diverge. The displacement range to achieve QZS (constant force) is 50 % to 55 % of the applied enforced displacement, i.e., ${}^l u = 0.5^l u$ and ${}^m u = 0.55^m u$.

The optimized topologies in Fig. 3(a)–(c) comprise a thin beam-like part next to the symmetry axis to provide positive stiffness in the vertical direction and an oblique part to possibly provide negative stiffness. It is observed that the designs with identical spring stiffness k_{Spring} have similar width of the beam-like part, and the angle of the oblique part and the location, shape, and size of the cavity at the top-right corner are affected by the magnitude of the enforced displacement u . The convergence histories of the objective function J of these three cases are plotted in Fig. 4(a), where the optimized objective function $J = 5.871, 6.088$, and 6.327 N/mm for Fig. 3(a)–(c) respectively. Fig. 4(a) indicates the iterative optimization processes are stable overall and converge fast, although some oscillations are observed. The possible cause of the oscillations could be the reaction force calculations in NFEA. In addition, the topologies for the design case in Fig. 3(a) at a number of iterations are listed in Table 2 to illustrate the evolution of topologies and material distributions from initially uniform material distribution, where It. represents the iteration.

It is observed that the objective function achieved for Fig. 3(a)–(c) are low ($\sim 6.0 \text{ N/mm}$) but not true quasi-zero. However, the force differences $\delta F = {}^m F - {}^l F$ of these cases are plotted in Fig. 4(b), which shows the forces are approximately constant ($\delta F < 1 \text{ N}$) in the displacement range). In addition, the force-displacement curves and stiffness of those designs require full NFEA simulations to validate the QZS behaviors in Section 4.

In addition, the choice of artificial spring stiffness is also studied. It should be noted that if a spring is too stiff, the boundary condition will approach fixed support. Hence, k_{Spring} of 4 and 5 N/mm are selected, and the coupled enforced displacement u should also be re-selected to avoid divergence in NFEA. The optimized topologies for $u = 12 \text{ mm}$ $k_{\text{Spring}} = 4 \text{ N/mm}$, $u = 11 \text{ mm}$ $k_{\text{Spring}} = 5 \text{ N/mm}$, and $u = 13 \text{ mm}$ $k_{\text{Spring}} = 5 \text{ N/mm}$ are depicted in Fig. 3(d)–(f), where their objective function values are 7.325, 8.173, and 7.808 N/mm . Compared with Fig. 3(a)–(c) with $k_{\text{Spring}} = 3 \text{ N/mm}$, a larger artificial spring stiffness can generally lead to a larger width of the beam-like vertical part connected to it.

This example demonstrates the effectiveness and efficiency of the present method to minimize the stiffness and produce structures with positive and negative stiffness elements to achieve QZS. However, a vertical spring appears in the optimized designs. While vertical springs can be easily integrated into the optimized design in both numerical and experimental tests, as well as in practical

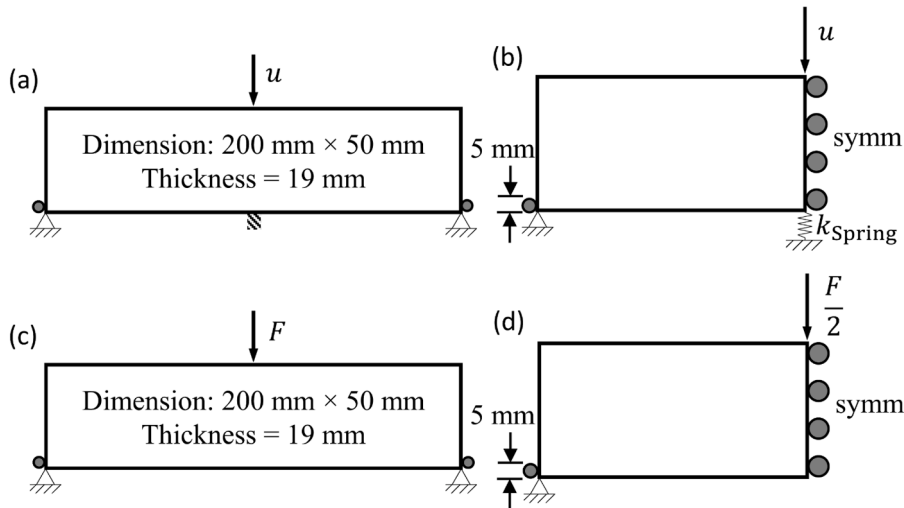


Fig. 2. Schematics of QZS metastructure design case studies (a) design domain and (b) computational model; and schematics of snap-through metastructure design case studies (c) design domain and (d) computational model.

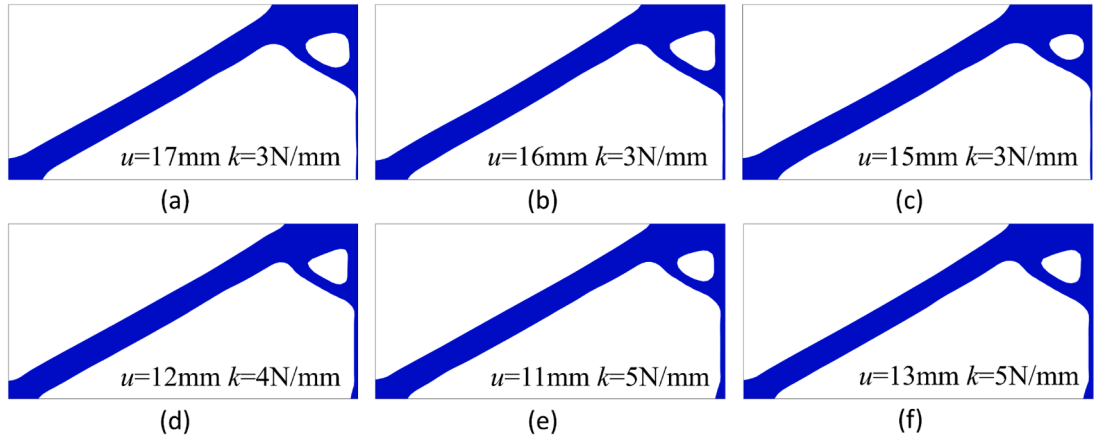


Fig. 3. QZS metastructure design problem: optimized topology of (a) enforced displacement $u = 17$ mm spring stiffness $k = 3$ N/mm, (b) $u = 16$ mm $k = 3$ N/mm, (c) $u = 15$ mm $k = 3$ N/mm, (d) $u = 12$ mm $k = 4$ N/mm, (d) $u = 11$ mm $k = 5$ N/mm, and (e) $u = 13$ mm $k = 5$ N/mm.

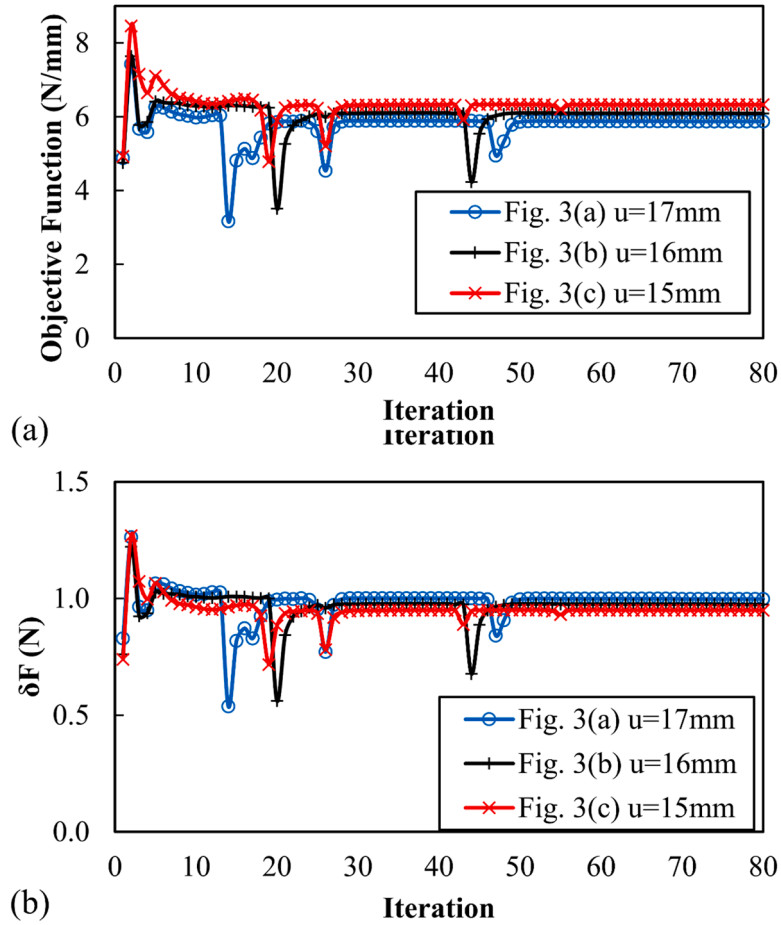





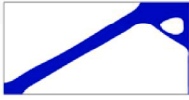





Fig. 4. QZS metastructure design problem: iterative histories of (a) the objective functions and (b) force differences for spring stiffness $k = 3$ N/mm and enforced displacement $u = 17$ mm (Fig. 3(a)), $u = 16$ mm (Fig. 3(b)), and $u = 15$ mm (Fig. 3(c)).

Table 2
Iterative histories of topologies for design case $k = 3\text{N/mm}$ and $u = 17\text{ mm}$ (Fig. 3(a)).

Iteration	Topology	Material distribution
It. 0 (Initialization)		
It. 1		
It. 5		
It. 20		
It. 40		

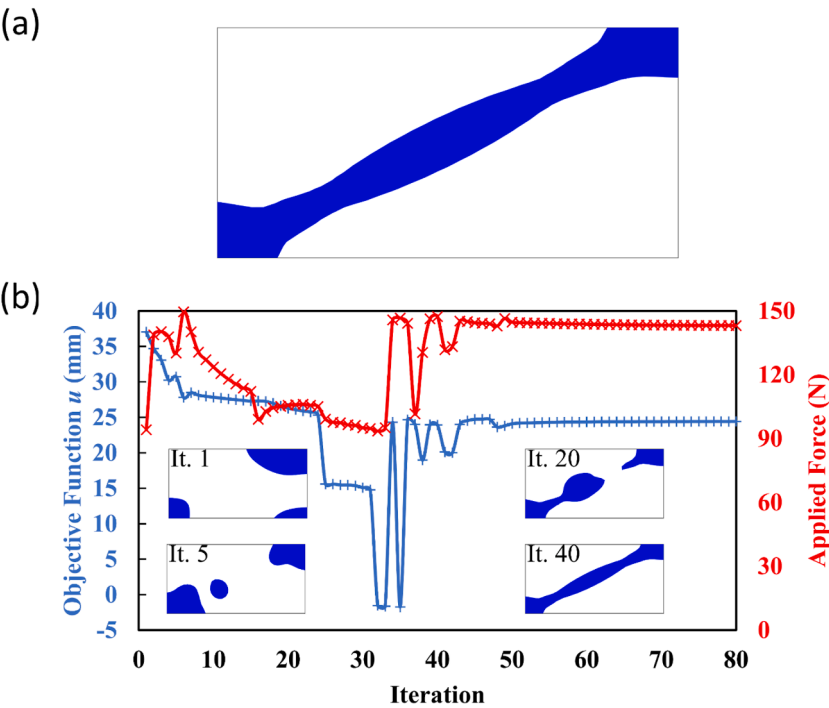


Fig. 5. Snap-through metastructure design problem: (a) optimized topology and (b) iterative histories of the objective function and applied load, with topologies at iteration (It.) 1, 5, 20, and 40.

applications for vibration isolators, we present an approach to remove the springs by restoring the fixed boundary condition, as discussed in Section 4.4.

3.2. Metastructures with snap-through feature

This example presents the design of metastructures with snap-through features. The design domain and computational model of the QZS design problem are revised for snap-through features and shown in Fig. 2(c) and (d), where an 80×40 mesh is applied. For the snap-through problem, a force instead of enforced displacement is applied, as formulated in Section 2.2, and the magnitude should be selected in a similar manner to the enforced displacement in the QZS problem. In NFEA for an applied force, an arc-length approach should be adopted to effectively deal with the negative stiffness.

The optimized topology for applied force $F = 150$ N is shown in Fig. 5(b). The structure layout is comparable to the curved beams with snap-through behaviors used in the existing QZS devices [11,18,25]. The convergence histories of the objective function are plotted in Fig. 5(b). It can be seen that the iterative optimization process is relatively stable with some oscillations. Since the arc-length approach is exploited in NFEA to deal with negative stiffness, the actual applied load at the final state is not 150 N. Thus, the computed displacements at the final state, i.e., the objective function, may oscillate until the optimal design is obtained. In addition, the actual applied loads at the final state are also plotted in Fig. 5(b) against iteration numbers.

The snap-through feature of this design will be tested in the next section. Please note this paper focuses on the experimental validation of snap-through structures and their use in synthesizing QZS metastructures, while the topology optimization of these structures is extended from our previous work [43]. Additional design cases involving bistable or multi-stable structures with snap-through features can also be referred to [43].

4. Numerical and experimental validation

In this section, metastructures with QZS or snap-through features are verified via numerical NFEA simulations and/or experimental tests. The QZS metastructure designs obtained using the present optimization method in Section 3.1 are numerically investigated and validated by NFEA; the snap-through structure obtained in Section 3.2 is experimentally studied and compared with NFEA simulations. Moreover, QZS metastructures composed of the optimized snap-through structure (as negative stiffness elements) are also numerically validated, as well as post-processed QZS metastructures without artificial springs.

4.1. Validation of QZS metastructures

The optimized QZS metastructures in Fig. 3 are validated via numerical NFEA simulations. The optimized topologies are converted to CAD models and imported to the FEA software NASTRAN. It should be noted that the mirror symmetry condition in topology optimization is not applied in the NFEA validation, as buckling of the vertical beam-like part may occur. Instead, the full-scale structures are numerically studied in NFEA, including the artificial spring. The boundary conditions are identical to those used in the structural optimization.

The NFEA results of the optimized structure in Fig. 3(a) are shown in Fig. 6. Fig. 6 plots the F - u curve of the NFEA results, where embedded figures show deformations and nonlinear von Mises stress distributions at displacements $u = 10, 20$, and 27 mm. If the enforced displacement is larger than 27 mm, the vertical beam-like part will buckle and lead to divergence of the NFEA. However, as the enforced displacement $u \leq 17$ mm in the topology optimization studies, the current computations are sufficient for validation purposes. The F - u curve in Fig. 6 indicates the design can achieve a quasi-zero 0.502 N/mm stiffness over a 17 mm range (10 to 27

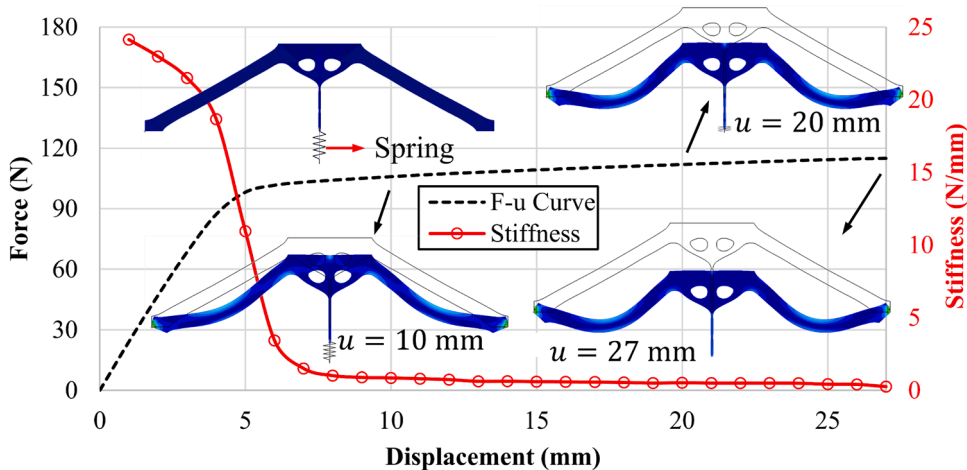


Fig. 6. Force-displacement curve and deformation with nonlinear von Mises stress contour of the optimized QZS metastructure in Fig. 3(a).

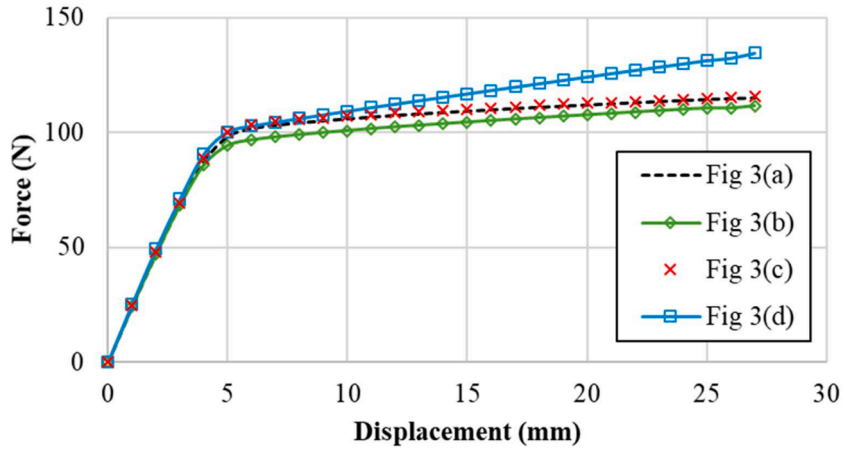


Fig. 7. Force-displacement curves of the optimized QZS metastructures in Fig. 3(a)–(d).

mm), and the objective function value calculated over the displacement range is 8.538 N/mm. It is evident that the proposed objective function can effectively achieve the QZS design objective. The stiffness given by $(^kF - ^{k-1}F)/(^k u - ^{k-1}u)$ are also plotted over displacement in Fig. 6, which shows the $F-u$ curve is approximately constant QZS.

Similarly, NFEA computations are conducted for the designs in Fig. 3(b)–(d), and the $F-u$ curves are plotted in Fig. 7. The stiffness for those designs are 0.630, 0.534, and 1.482 N/mm in the same displacement range of Fig. 6, while the objective function values over the displacement range are 10.717, 9.074, and 25.187 N/mm. The quasi-zero stiffness results from numerical simulations in this section validate the present QZS metastructure designs and the proposed optimization method. In the topology optimization, the case Fig. 3(a) obtains the lowest objective function values, and in the NFEA simulation, it also shows the lowest stiffness among all design cases, which also confirms the validity of the optimization method.

Figs. 6 and 7 show that the optimal designs of metastructures with constant QZS are successfully obtained using the present formulation and algorithm. Although the optimized designs include a vertical spring, it is worth noting that in vibration isolator applications for QZS structures, vertical springs are commonly utilized and can be easily integrated with the optimized design in practice. However, we present an approach to remove the springs, as discussed in Section 4.4.

4.2. Validation of snap-through metastructures

The optimized design for snap-through features in Fig. 5(a) is fabricated, and its snap-through behaviors are experimentally tested. The measured $F-u$ curves and deformation are compared with those computed by NFEA.

The optimized design in Fig. 5(a) was fabricated using polyurethane (ET90A+MOCA), whose material properties are given in Table 1. The specimens, with dimensions shown in Fig. 8(a), were cut from polyurethane plates using waterjet technology. Aluminum sheets were bonded to the left and right side surfaces of the specimens to facilitate the experimental setup. Fig. 8(b) shows the setup, where clamps fix the specimens, ensuring that only the curved sections deform during loading and unloading, while the straight sections experience minor to no deformation.

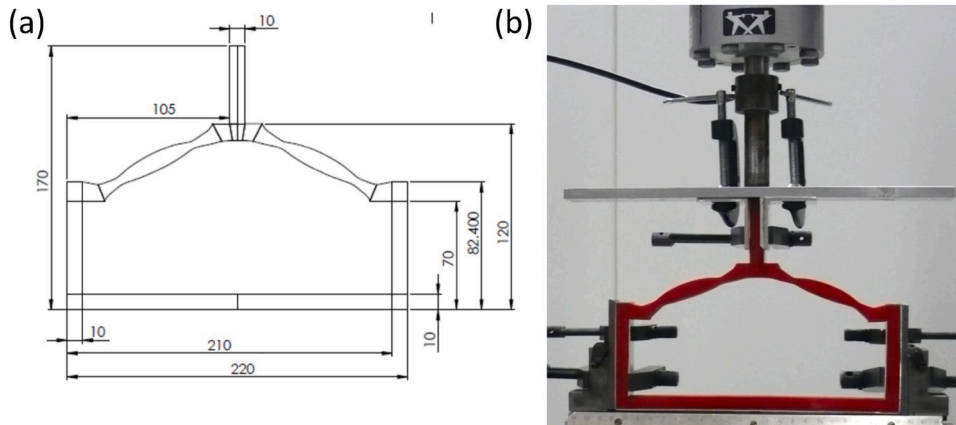


Fig. 8. Experimental testing of snap-through metastructure (a) dimension of specimens and (b) experimental setup.

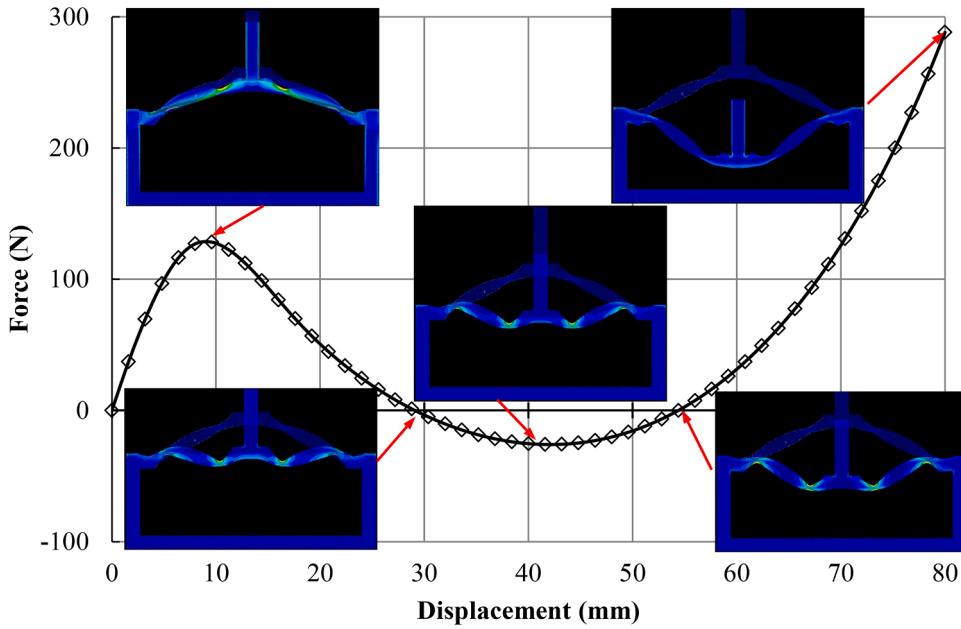


Fig. 9. Snap-through behaviors of the specimen where embedded figures present deformation with nonlinear von Mises stress contour at characteristic points.

Before testing, the NFEA simulation is conducted using NASTRAN. Material nonlinearity of the aluminum sheets is neglected as their deformations are small and linear. Loading and boundary conditions are identical to the experimental tests. The F - u curve of the NFEA results is plotted in Fig. 9, where embedded figures show deformations and nonlinear von Mises stress distributions at 5 characteristic points at $F = F_{c1}$, 0 (unstable state), F_{c2} , 0 (2nd stable state), and nF (final state). The F - u curve indicates that snap-through as well as bistable state behaviors can be achieved.

The experiment testing was conducted in the versatile testing machine INSTRON-3366. In the experimental testing, loading and unloading rates were 5 mm/min; the displacement-controlled testing was programmed in the testing software Bluehill 3 so that compressive and tensile forces could be recorded and unloading curves could be obtained.

Fig. 10 illustrates the F - u curves measured in the experiment. The curve of loading and unloading was obtained in the test with a maximum displacement of 80 mm, consistent with the NFEA. In Fig. 10, the F - u curve and deformation predicted by NFEA are also given. By observing the F - u curve and embedded image at $F \approx F_{c2}$ obtained in the experiment and those predicted by the NFEA, it can be seen that the NFEA results correlate well with those recorded in the experiment. Both the NFEA and experimental results reveal the negative stiffness, snap-through and bistable state behaviors of the optimized design. The good correlation between the experimental and FEA results also shows the reliability of the FEA validation for the QZS metastructure in Section 4.1.

In addition, it is observed that the optimized design exhibits the hysteretic behavior, as shown in the loading and unloading curve in Fig. 10. Since the present study focuses on quasi-static validations, hysteresis effects are not considered in the numerical analysis. However, hysteresis is a critical factor that should be taken into account in dynamic analysis.

4.3. Synthesis of QZS metastructures and validation

Since the previous section proves the snap-through and negative stiffness behaviors of the optimized snap-through metastructure in Fig. 5(a), the design is exploited to synthesize QZS metastructures. The optimized design with negative stiffness is combined with a vertical bar of width D to provide positive stiffness, as depicted in Fig. 11(b), and the corresponding combination of their F - u curves is shown in Fig. 11(a). The synthesized full-scale structures (see Fig. 11(c)) with different widths D are numerically studied in NFEA.

The NFEA results for the case $D = 0.5$ mm are plotted in Fig. 12, including the F - u curve and deformations and nonlinear von Mises stress distributions at displacements $u = 10$, 15, and 22 mm. It is observed that the vertical beam-like part starts to buckle at the enforced displacement $u = 22$ mm. Therefore, as divergence occurs, no further NFEA results are presented beyond this point. The F - u curve indicates the design can achieve a quasi-zero stiffness of 0.402 N/mm in a range of 12 mm (10 to 22 mm).

Different choices of width D are also numerically computed, as shown in Fig. 13. The stiffness obtained for $D = 0.6$ mm and 0.8 mm are 1.719 and 4.373 N/mm, respectively. Evidently, the positive stiffness of the beam should exactly balance the negative stiffness of the snap-through structure. It is realized in the $D = 0.5$ mm case, while the larger widths in other cases result in too high positive stiffness. In practice, the positive stiffness elements should be carefully calculated based on the F - u curve of the negative stiffness component (e.g., Fig. 10). The coupling between the positive and negative stiffness elements could provide guidance for the selection of the width D . Thus, to avoid this further calculation, the direct topology optimization method is recommended as compared to the

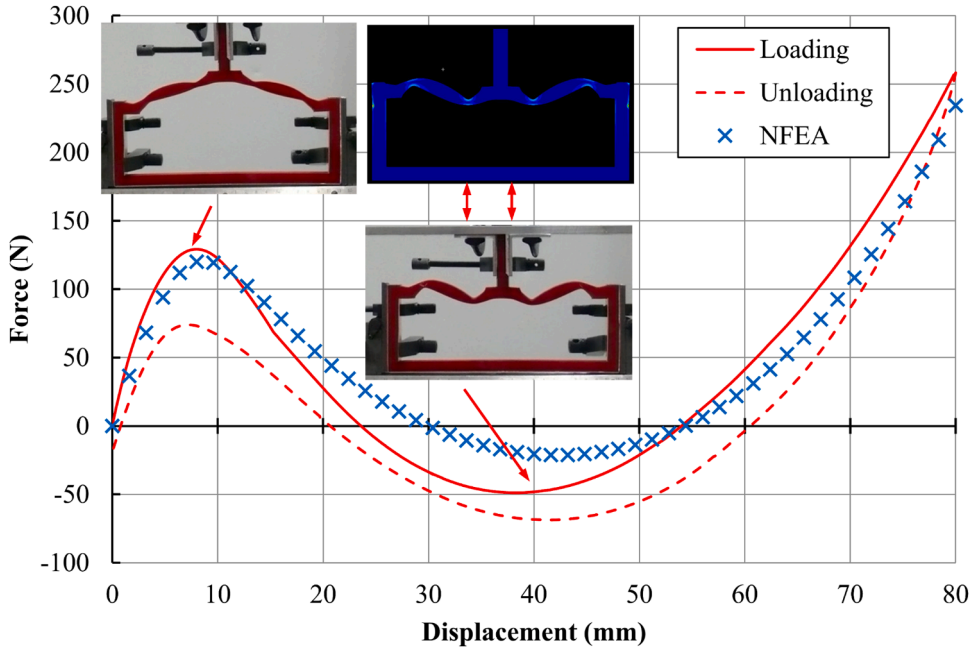


Fig. 10. Results measured in the experiment and predicted by the NFEA for the snap-through metastructure design where the embedded figure present deformation for Loading at $F \approx F_{c1}$ and $F \approx F_{c2}$ and for NFEA simulation at $F \approx F_{c2}$.

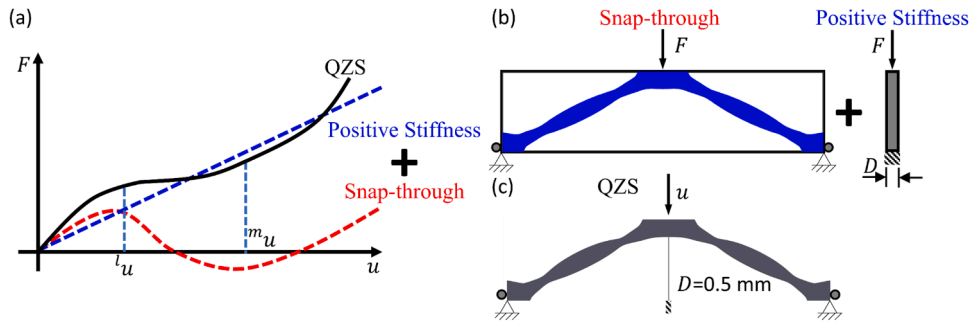


Fig. 11. Synthesis of QZS metastructure by combining snap-through metastructures with positive stiffness elements: (a) combining force-displacement curves, (b) combining structures, and (c) synthesized design.

synthesis method.

4.4. Extension: removal of artificial springs for optimized QZS metastructures and validation

The proposed optimization method can produce metastructures with QZS characteristics but initially involves the artificial spring. This section extends the present method by introducing an approach to remove the spring. As discussed in Section 3.1, the spring is employed to approximate the fixed boundary condition. Thus, the spring could be removed by restoring the fixed boundary condition.

To effectively adjust the structures based on boundary conditions, the equivalence of displacements must be maintained. As shown in Fig. 14(c), for both the original and adjusted designs, the vertical (y-axis) displacements should be consistent. This can be simplified to ensuring equivalent axial displacements in the beam-like part. Hence, the adjustment focuses on modifying the width of the beam-like segment by considering the equivalence of axial displacements:

$$\frac{NL}{EDT} + \frac{N}{k_{\text{Spring}}} = \frac{NL}{ED^*T} \quad (20)$$

where N denotes the axial force; E represents Young's modulus; L is the length of the beam; D and D^* are the original and adjusted width (assume constant along L) of the beam; and T is the thickness of the beam.

The adjustment presented in Fig. 14 is based on the designs in Fig. 3(a), where $k_{\text{Spring}} = 3 \text{ N/mm}$. The adjusted D^* in Fig. 14(b),

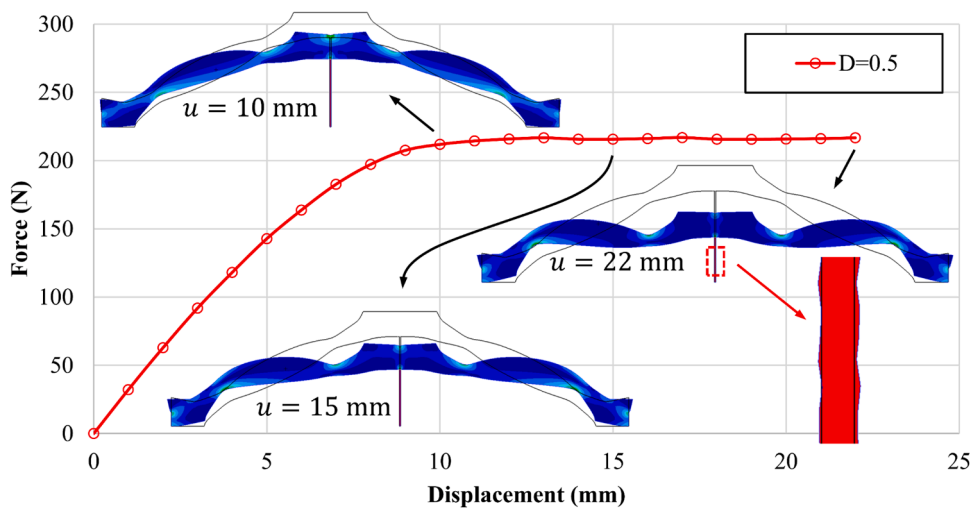


Fig. 12. Force-displacement curve and deformation with nonlinear von Mises stress contour of the synthesized QZS metastructure with width $D = 0.5$ mm.

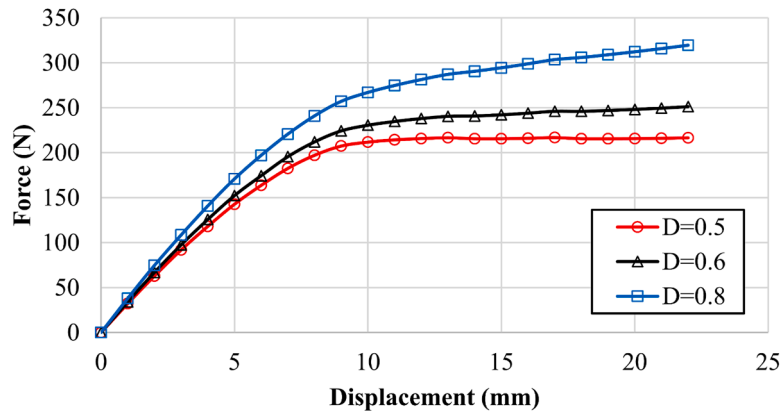


Fig. 13. Force-displacement curves of the synthesized QZS metastructure with different widths $D = 0.5, 0.6$, and 0.8 mm.

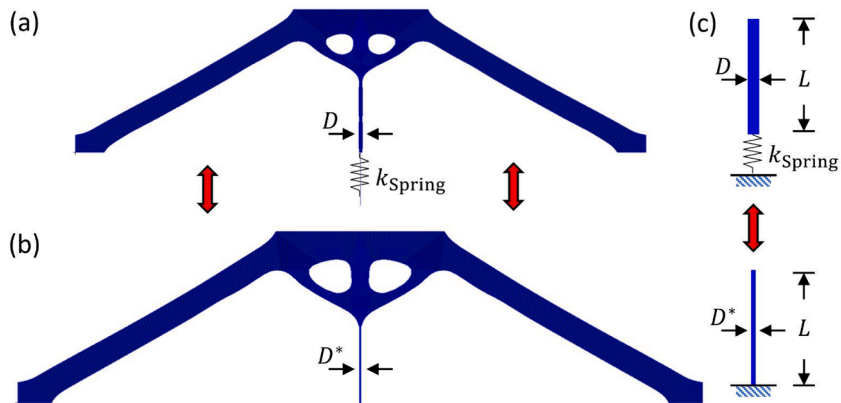


Fig. 14. Post-processing of QZS metastructure (a) original optimized design with spring and (b) adjusted single-part design; and (c) boundary conditions of the original and adjusted designs.

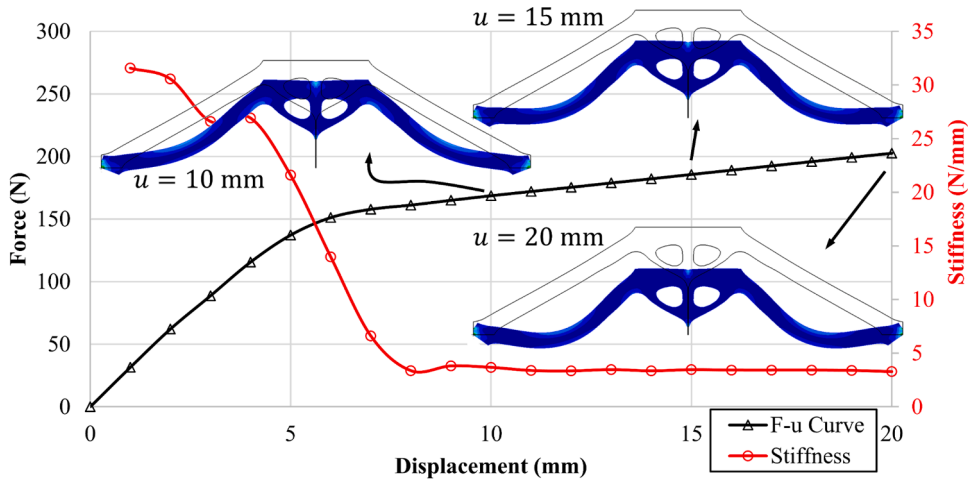


Fig. 15. Force-displacement curve and deformation with nonlinear von Mises stress contour of the adjusted QZS metastructure with width $D^*=0.3$ mm.

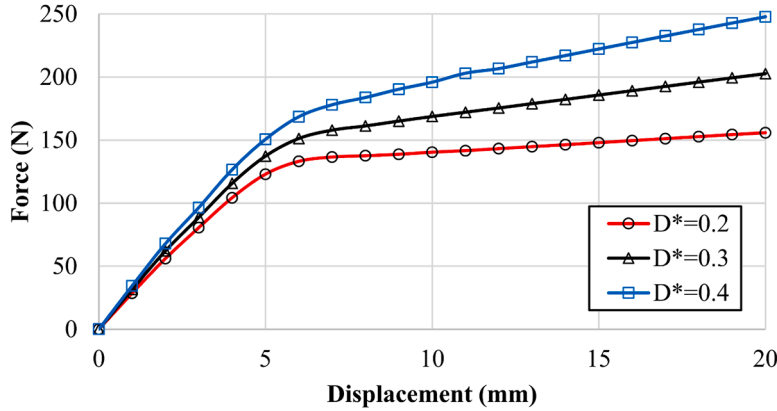


Fig. 16. Force-displacement curve of the adjusted QZS metastructure with width $D^*=0.3$ mm and comparisons with $D^*=0.2$ and 0.4 mm.

estimated using Eq. (20), is 0.3 mm, which is numerically simulated via NFEA. Fig. 15 plots the $F-u$ curve obtained from the NFEA, along with the deformations and nonlinear von Mises stress distributions, at displacements $u = 10, 15$, and 20 mm. The NFEA results show that the stiffness compromises to 3.392 N/mm (compared to the original design of 0.502 N/mm) due to the removal of the spring. The stiffness given by $(k_F - k^{-1}F)/(k_u - k^{-1}u)$ are also plotted over displacement in Fig. 15. The value is small and nearly constant, though not true quasi-zero.

In addition, other selections of width $D^*=0.2$ and 0.4 mm are also numerically investigated for comparison purposes. The $F-u$ curves are depicted in Fig. 16, where the stiffness obtained for $D^*=0.2$ and 0.4 mm are 1.544 and 5.188 N/mm, respectively. It is evident that the adjustment effectively removes the spring while maintaining low stiffness. However, further fine-tuning of D^* may be needed in practice to achieve true quasi-zero stiffness.

The zero stiffness of the optimal designs of the metastructure with QZS feature and the modified designs by removing the artificial spring have not been obtained, but the stiffness is sufficiently low for a vibration isolator with high-static and low-dynamic stiffness. Additionally, as the low stiffnesses shown in Figs. 13 and 16 are almost constant, the obtained metastructures can be applied in vibration isolation systems with variable mass and could potentially solve the challenge of vibration isolation for variable mass using QZS isolators.

5. Conclusions

This study investigates the topology optimization of QZS metastructure designs. We propose (1) mathematical formulations of the objective function based on the QZS force-displacement curve; (2) novel and generalized mathematical formulations of the optimization problem using force and displacement expressed in terms of stress and strain of all load steps in NFEA; and (3) an extended moving isosurface threshold (MIST) method to solve the formulated optimization problem. Additionally, mathematical formulations

and optimization method are also presented for snap-through features, as well as a design approach that synthesizes QZS metastructures by exploiting snap-through behaviors. Based on the obtained numerical and experimental results, the following conclusions could be drawn: Based on the obtained numerical and experimental results, the following conclusions could be drawn: (1) the derived theoretical formulation and optimization algorithm can effectively optimize the design of structures with QZS, as metastructures with constant QZS are successfully obtained using the present formulation and algorithm; (2) negative stiffness, snap-through, and bistable state behaviors of the optimized design are observed in both numerical simulations and experimental tests, demonstrating the effectiveness of the optimization method for the snap-through features; (3) it is feasible to synthesize QZS structures on the basis of the snap-through and QZS with an artificial spring, as constant QZS is achieved in the synthesized metastructures using snap-through structures and QZS structures by removing an artificial spring.

It is important to note that the present work focuses on proposing the problem formulation for metastructures with QZS features and presenting a solution method via the MIST, while the optimized QZS metastructures are validated only through FEA simulations, as experiments have not been conducted. However, for the snap-through metastructures, both FEA and experimental validations have been performed. Fig. 10 shows a good correlation between the experimental and FEA results for the snap-through metastructure, supporting the reliability of the FEA simulations for validating the QZS metastructure. In future work, static and dynamic tests will be carried out for the QZS metastructures obtained by topology optimization for vibration isolation.

CRedit authorship contribution statement

Yifu Lu: Writing – original draft, Visualization, Methodology, Conceptualization. **Quantian Luo:** Writing – review & editing, Software, Methodology, Conceptualization. **Liyong Tong:** Writing – review & editing, Supervision, Funding acquisition.

Declaration of competing interest

The authors declare that they have no known competing financial interests or personal relationships that could have appeared to influence the work reported in this paper.

Acknowledgments

The authors are grateful for the support of the Australian Research Council via Discovery-Project Grants DP170104916.

Appendix

This section presents the numerical implementations of the MIST method, as well as detailed solution procedures. The iterative solution procedures implemented by MATLAB are illustrated as follows, with I being the iteration number.

Step 1: Initialization

- Define design domains Ω^0 and design variables x_e^0 .
- Define FEA parameters.
- Define solver parameters: material penalty factor p ; initial dynamic move limit k_{mv}^0 ; x_{\min} ; prescribed volume fraction V_f ; and filter radius r_{\min} .

Step 2: Structural analysis (NFEA)

- Update material properties by:

$$D_e(x_e) = x_e^p D^0(A1)$$

where D_e and D^0 denote the elasticity/constitutive matrix of the e^{th} element and that of the base solid material; p is the material penalty factor.

For the QZS problem:

- Solve nonlinear analysis subjected to enforced displacement:
- Extract ${}^k\epsilon_{ij}$ and ${}^kS_{ij}$, and kF ($k = 1, 2, \dots, n$).

For the snap-through problem:

- Solve nonlinear analysis subjected to applied force.
- Extract ${}^k\epsilon_{ij}$, ${}^kS_{ij}$ ($k = 1, 2, \dots, n$).

Step 3: Update topology and design variables

- Calculate the response function Φ^I by Eq. (16) for QZS feature or Eq. (17) for snap-through feature; filtered with radius r_{\min} ; and normalized.
- Determine the threshold level t^I by a standard bisection method for the prescribed volume fractions V_f .
- Intersect the 3D surface Φ^I and isosurface t^I , and generate the topologies Ω^I and design variables $(x_e^I)^0$ by Eq. (19).
- Updated design variables x_e^I in a relaxed form:

$$\bar{x}_e^I = x_e^{I-1} + k_{mv} \left((x_e^I)^0 - x_e^{I-1} \right) \quad (\text{A2a})$$

$$x_e^I = \begin{cases} \bar{x}_e^I, & \text{for } \bar{x}_e^I \geq x_{\min} \\ 0, & \text{for } \bar{x}_e^I < x_{\min} \end{cases} \quad (\text{A2b})$$

where k_{mv} is the dynamic move limit, which is halved when an oscillation of objective function occurs until k_{mv} reaches the $1/2^3$ of k_{mv}^0 . Eq. (A2b) indicates the removal of low-density elements from NFEA [54] with the criterion $\bar{x}_e^I < x_{\min}$.

Step 4: Termination check

- Calculate termination criteria:

$$\Delta\Phi^I = \frac{1}{V_f N_n} \left[\sum_{r_n=1}^{N_n} |\Phi^I(r_n) - \Phi^{I-1}(r_n)| \right] \quad (\text{A3})$$

where $\Phi^k(r_n)$ is the Φ value at node r_n and N_n is the total number of nodes.

- If the difference $\Delta\Phi^k$ reaches a criterion value (e.g., 10^{-3}) and/or a certain number of iterations (e.g., 100) are reached, the iterative optimization procedures terminate. Otherwise, the iteration will go back to Step 2 with $I = I + 1$.

Data availability

The necessary information for replicating the results is presented in the manuscript. Further details regarding the implementation are available upon request from the corresponding author.

References

- [1] R. Ma, K. Bi, H. Hao, Inerter-based structural vibration control: a state-of-the-art review, *Eng. Struct.* 243 (2021) 112655.
- [2] Z. Lu, Z. Wang, Y. Zhou, X. Lu, Nonlinear dissipative devices in structural vibration control: a review, *J. Sound Vib.* 423 (2018) 18–49.
- [3] P.S. Balaji, K.K. SelvaKumar, Applications of nonlinearity in passive vibration control: a review, *J. Vib. Eng. Technol.* 9 (2021) 183–213.
- [4] R. Ibrahim, Recent advances in nonlinear passive vibration isolators, *J. Sound Vib.* 314 (2008) 371–452.
- [5] A. Carrella, M. Brennan, T. Waters, Static analysis of a passive vibration isolator with quasi-zero-stiffness characteristic, *J. Sound Vib.* 301 (2007) 678–689.
- [6] G. Gatti, A nonlinear quasi-zero stiffness vibration isolator with quintic restoring force characteristic: a fundamental analytical insight, *J. Vib. Control* 30 (2024) 4185–4198.
- [7] F. Zhao, J. Ji, K. Ye, Q. Luo, An innovative quasi-zero stiffness isolator with three pairs of oblique springs, *Int. J. Mech. Sci.* 192 (2021) 106093.
- [8] K. Yu, Y. Chen, C. Yu, J. Zhang, X. Lu, A compact nonlinear stiffness-modulated structure for low-frequency vibration isolation under heavy loads, *Nonlinear Dyn.* 112 (2024) 5863–5893.
- [9] X. Sun, X. Jing, Analysis and design of a nonlinear stiffness and damping system with a scissor-like structure, *Mech. Syst. Signal Process.* 66 (2016) 723–742.
- [10] C. Zhou, G. Sui, Y. Chen, X. Shan, A nonlinear low frequency quasi zero stiffness vibration isolator using double-arc flexible beams, *Int. J. Mech. Sci.* (2024) 276.
- [11] J. Liu, Y. Wang, S. Yang, T. Sun, M. Yang, W. Niu, Customized quasi-zero-stiffness metamaterials for ultra-low frequency broadband vibration isolation, *Int. J. Mech. Sci.* (2024) 269.
- [12] C. Liu, R. Zhao, K. Yu, H.P. Lee, B. Liao, A quasi-zero-stiffness device capable of vibration isolation and energy harvesting using piezoelectric buckled beams, *Energy* 233 (2021) 121146.
- [13] X. Huang, X. Liu, J. Sun, Z. Zhang, H. Hua, Vibration isolation characteristics of a nonlinear isolator using Euler buckled beam as negative stiffness corrector: a theoretical and experimental study, *J. Sound Vib.* 333 (2014) 1132–1148.
- [14] X. Sun, F. Wang, J. Xu, Analysis, design and experiment of continuous isolation structure with Local Quasi-Zero-Stiffness property by magnetic interaction, *Int. J. Non Linear Mech.* 116 (2019) 289–301.
- [15] B. Yan, H. Ma, C. Zhao, C. Wu, K. Wang, P. Wang, A vari-stiffness nonlinear isolator with magnetic effects: theoretical modeling and experimental verification, *Int. J. Mech. Sci.* 148 (2018) 745–755.
- [16] Q. Zhang, S. Xia, D. Xu, Z. Peng, A torsion–translational vibration isolator with quasi-zero stiffness, *Nonlinear Dyn.* 99 (2020) 1467–1488.
- [17] K. Wang, J. Zhou, D. Xu, H. Ouyang, Tunable low-frequency torsional-wave band gaps in a meta-shaft, *J. Phys. D Appl. Phys.* 52 (2018) 055104.
- [18] S. Dalela, P.S. Balaji, D.P. Jena, Design of a metastructure for vibration isolation with quasi-zero-stiffness characteristics using bistable curved beam, *Nonlinear Dyn.* 108 (2022) 1931–1971.

- [19] B. Yan, H. Ma, B. Jian, K. Wang, C. Wu, Nonlinear dynamics analysis of a bi-state nonlinear vibration isolator with symmetric permanent magnets, *Nonlinear Dyn.* 97 (2019) 2499–2519.
- [20] W. Dai, B. Carboni, G. Quaranta, Y. Pan, W. Lacarbonara, Nonlinear response of a multidirectional negative-stiffness isolation system via semirecursive multibody dynamic approach, *Int. J. Mech. Syst. Dyn.* (2024).
- [21] J. Ji, Q. Luo, K. Ye, Vibration control based metamaterials and origami structures: a state-of-the-art review, *Mech. Syst. Signal Process.* 161 (2021) 107945.
- [22] Q. Zhang, D. Guo, G. Hu, Tailored mechanical metamaterials with programmable quasi-zero-stiffness features for full-band vibration isolation, *Adv. Funct. Mater.* (2021) 31.
- [23] P. Banerjee, S. Dalela, P.S. Balaji, S. Murugan, L.A. Kumaraswamidhas, Simultaneous vibration isolation and energy harvesting using quasi-zero-stiffness-based metastructure, *Acta Mech.* 234 (2023) 3337–3359.
- [24] H. Fan, L. Yang, Y. Tian, Z. Wang, Design of metastructures with quasi-zero dynamic stiffness for vibration isolation, *Compos. Struct.* (2020) 243.
- [25] X. Zhang, X. Lu, C. Li, R. Tian, L. Chen, M. Wang, Design of hyperbolic quasi-zero stiffness metastructures coupled with nonlinear stiffness for low-frequency vibration isolation, *Eng. Struct.* (2024) 312.
- [26] A. Valeev, A. Zotov, S. Kharisov, Designing of compact low frequency vibration isolator with quasi-zero-stiffness, *J. Low Freq. Noise Vib. Act. control* 34 (2015) 459–473.
- [27] X. Liu, S. Chen, B. Wang, X. Tan, L. Yu, A compact quasi-zero-stiffness mechanical metamaterial based on truncated conical shells, *Int. J. Mech. Sci.* (2024) 277.
- [28] H. Pu, J. Liu, M. Wang, J. Ding, Y. Sun, Y. Peng, J. Luo, Bio-inspired quasi-zero stiffness vibration isolator with quasilinear negative stiffness in full stroke, *J. Sound Vib.* 574 (2024).
- [29] C. Liu, W. Zhang, K. Yu, T. Liu, Y. Zheng, Quasi-zero-stiffness vibration isolation: designs, improvements and applications, *Eng. Struct.* (2024) 301.
- [30] M. Otomori, T. Yamada, K. Izui, S. Nishiwaki, J. Andkjær, A topology optimization method based on the level set method for the design of negative permeability dielectric metamaterials, *Comput. Methods Appl. Mech. Eng.* 237–240 (2012) 192–211.
- [31] S. Zhou, W. Li, Y. Chen, G. Sun, Q. Li, Topology optimization for negative permeability metamaterials using level-set algorithm, *Acta Mater.* 59 (2011) 2624–2636.
- [32] A.R. Diaz, O. Sigmund, A topology optimization method for design of negative permeability metamaterials, *Struct. Multidiscip. Optim.* 41 (2010) 163–177.
- [33] P. Vogiatzis, S. Chen, X. Wang, T. Li, L. Wang, Topology optimization of multi-material negative Poisson's ratio metamaterials using a reconciled level set method, *Comput. Aided Des.* 83 (2017) 15–32.
- [34] H. Zhang, Y. Luo, Z. Kang, Bi-material microstructural design of chiral auxetic metamaterials using topology optimization, *Compos. Struct.* 195 (2018) 232–248.
- [35] L. Lu, T. Yamamoto, M. Otomori, T. Yamada, K. Izui, S. Nishiwaki, Topology optimization of an acoustic metamaterial with negative bulk modulus using local resonance, *Finite Elem. Anal. Des.* 72 (2013) 1–12.
- [36] H.W. Dong, S.D. Zhao, Y.S. Wang, C. Zhang, Topology optimization of anisotropic broadband double-negative elastic metamaterials, *J. Mech. Phys. Solids* 105 (2017) 54–80.
- [37] L. Wang, J. Boddapati, K. Liu, P. Zhu, C. Daraio, W. Chen, Mechanical cloak via data-driven aperiodic metamaterial design, *Proc. Natl. Acad. Sci.* 119 (2022) e2122185119.
- [38] Y. Lu, L. Tong, Concurrent multiscale topology optimization of metamaterials for mechanical cloak, *Comput. Methods Appl. Mech. Eng.* 409 (2023) 115966.
- [39] K. Hirasawa, I. Nakami, T. Ooinoue, T. Asaoka, G. Fujii, Experimental demonstration of thermal cloaking metastructures designed by topology optimization, *Int. J. Heat Mass Transf.* 194 (2022) 123093.
- [40] Y. Huang, D. Wu, K. Zhang, H. Yang, W. Dong, M. Chen, D. Fang, Topological designs of mechanical-electromagnetic integrated laminate metastructure for broadband microwave absorption based on bi-directional evolutionary optimization, *Compos. Sci. Technol.* 213 (2021) 108898.
- [41] O. Abdeljaber, O. Avci, D.J. Inman, Optimization of chiral lattice based metastructures for broadband vibration suppression using genetic algorithms, *J. Sound Vib.* 369 (2016) 50–62.
- [42] Y. Xu, H.W. Dong, Y.S. Wang, Topology optimization of programable quasi-zero-stiffness metastructures for low-frequency vibration isolation, *Int. J. Mech. Sci.* (2024) 280.
- [43] Q. Luo, L. Tong, Optimal design of bi-and multi-stable compliant cellular structures, in: *Proceedings of the International Design Engineering Technical Conferences and Computers and Information in Engineering Conference*, American Society of Mechanical Engineers, 2018. V05AT07A009.
- [44] T.E. Bruns, O. Sigmund, Toward the topology design of mechanisms that exhibit snap-through behavior, *Comput. Methods Appl. Mech. Eng.* 193 (2004) 3973–4000.
- [45] E. Lindgaard, J. Dahl, On compliance and buckling objective functions in topology optimization of snap-through problems, *Struct. Multidiscip. Optim.* 47 (2013) 409–421.
- [46] K.A. James, H. Waisman, Layout design of a bi-stable cardiovascular stent using topology optimization, *Comput. Methods Appl. Mech. Eng.* 305 (2016) 869–890.
- [47] Y. Huang, J. Zhao, S. Liu, Design optimization of segment-reinforced bistable mechanisms exhibiting adjustable snapping behavior, *Sens. Actuators A Phys.* 252 (2016) 7–15.
- [48] H. Deng, L. Cheng, X. Liang, D. Hayduke, A.C. To, Topology optimization for energy dissipation design of lattice structures through snap-through behavior, *Comput. Methods Appl. Mech. Eng.* 358 (2020) 112641.
- [49] A. Bhattacharyya, C. Conlan-Smith, K.A. James, Design of a Bi-stable airfoil with tailored snap-through response using topology optimization, *Comput. Aided Des.* 108 (2019) 42–55.
- [50] K.J. Bathe, *Finite Element Procedures*, Prentice Hall, Englewood Cliffs, N.J., 1996, p. c1996.
- [51] R.D. Cook, D.S. Malkus, M.E. Plesha, *Concepts and Applications of Finite Element Analysis*, 4th ed., Wiley, New York, 2001, p. c2001, 4th edition.
- [52] L.Y. Tong, J.Z. Lin, Structural topology optimization with implicit design variable-optimality and algorithm, *Finite Elem. Anal. Des.* 47 (2011) 922–932.
- [53] S. Vasista, L. Tong, Topology optimisation via the moving iso-surface threshold method: implementation and application, *Aeronaut. J.* 118 (2014) 315–342.
- [54] Q. Luo, L. Tong, An algorithm for eradicating the effects of void elements on structural topology optimization for nonlinear compliance, *Struct. Multidiscip. Optim.* 53 (2016) 695–714.